Nanoscale

A Type-I van der Waals Heterostructure formed by Monolayer WS2 and Trilayer PdSe2

Journal:	*Nanoscale*
Manuscript ID	NR-ART-06-2024-002664.R1
Article Type:	Paper
Date Submitted by the Author:	24-Aug-2024

Complete List of Authors:	Li, Guili; Beijing Jiaotong University, Zhang, Xiaoxian; Beijing Jiaotong University, Institute of Optoelectronic Technology Wang, Yongsheng; Key Laboratory of Luminescence and Optical Information, Ministry of Education, Institute of Optoelectronic Technology, Beijing Jiaotong University, Liu, XiaoJing; Key Laboratory of Luminescence and Optical Information, Ministry of Education,Institute of Optoelectronic Technology, Beijing Jiaotong University Ren, Fangying; Beijing Jiaotong University, Beijing He, Jiaqi; Beijing University of Chemical Technology, He, Dawei; Beijing Jiaotong University, Key Laboratory of Luminescence and Optical Information Zhao, Hui; University of Kansas, Physics and Astronomy

Journal Name

ARTICLE TYPE

Cite this: DOI: 00.0000/xxxxxxxxxx

A Type-I van der Waals Heterostructure formed by Monolayer WS_2 and Trilayer $PdSe_2$

Guili Li,[a] Xiaoxian Zhang,[a] Yongsheng Wang,[a] XiaoJing Liu,[a] FangYing Ren,[a] Jiaqi He,*[b] Dawei He *[a] and Hui Zhao*[c]

Received Date
Accepted Date

DOI: 00.0000/xxxxxxxxxx

Two-dimensional (2D) heterostructures, formed by stacking 2D semiconductors through the van der Waals force, have been extensively studied recently. However, the majority of the heterostructures discovered so far possess type-II interfaces that facilitate interlayer charge separation. Type-I interfaces, on the other hand, confine both electrons and holes in one layer, which is beneficial for optical applications that utilize electron-hole radiative recombination. So far, only a few type-I 2D heterostructures have been achieved, which has limited the construction of multilayer heterostructures with sophisticated band landscapes. Here, we report experimental evidence of a type-I interface between monolayer WS_2 and trilayer $PdSe_2$. Two-dimensional $PdSe_2$ has emerged as a promising material for infrared optoelectronic and other applications. We fabricated the heterostructure by stacking an exfoliated monolayer WS_2 flake on top of a trilayer $PdSe_2$ film, synthesized by chemical vapor deposition. Photoluminescence spectroscopy measurements revealed that the WS_2 exciton peak is significantly quenched in the heterostructure, confirming efficient excitation transfer from WS_2 to $PdSe_2$. Femtosecond transient absorption measurements with various pump/probe configurations showed that both electrons and holes photoexcited in the WS_2 layer of the heterostructure can efficiently transfer to $PdSe_2$, while neither type of carriers excited in $PdSe_2$ can transfer to WS_2. These experimental findings establish a type-I band alignment between monolayer WS_2 and trilayer $PdSe_2$. Our results further highlight $PdSe_2$ as an important 2D material for constructing van der Waals heterostructures with emergent electronic and optoelectronic properties.

1 Introduction

Recently, studies on two-dimensional (2D) layered materials have revealed the formation of van der Waals (vdW) heterostructures through the stacking of different material layers *via* vdW forces. These heterostructures offer several advantages for device applications [1–4], including flexible energy band tuning, precise control over charge carrier transport and layer population, integration of multiple functionalities, and tunable interfacial properties. Unlike traditional interfaces, vdW interfaces do not require lattice matching, enabling the creation of numerous novel artificial materials and transforming material discovery. The energy band alignment is a crucial characteristic that determines the electronic and optical properties of vdW heterostructures. In heterostructures with type-I band alignment, the conduction band minimum (CBM) of the narrow-gap material is lower than that of the wide-gap material, while its valence band maximum (VBM) is higher than that of the wide-gap material. As a result, both electrons and holes can transfer from the wide-gap material to the narrow-gap material, as depicted in Figures 1a and 1b. This type of band alignment facilitates electron-hole recombination in the narrow-gap material, making it advantageous for light-emission applications [5]. In contrast, type-II heterostructures exhibit a band alignment where both the CBM and VBM of one material are higher than those of the other material. This band offset allows electrons and holes to transfer in opposite directions, leading to interfacial charge separation, as illustrated in Figure 1c and Figure 1d. This feature is particularly attractive for optoelectronic devices such as photovoltaics and photodetectors [6–9].

Currently, the majority of studied vdW heterostructures exhibit type-II band alignments. Notably, all combinations involving the four extensively examined transition metal dichalcogenides (TMDs), MoS_2, WS_2, $MoSe_2$, and WSe_2, display type-II characteristics, showcasing unique charge transfer properties. In contrast, only a limited number of type-I vdW heterostructures

[a] *Key Laboratory of Luminescence and Optical Information, Ministry of Education, Institute of Optoelectronic Technology, Beijing Jiaotong University, Beijing 100044, China. E-mail: dwhe@bjtu.edu.cn*
[b] *College of Mathematics and Physics, Beijing University of Chemical Technology, Beijing 100029, China. E-mail: jqhe@buct.edu.cn*
[c] *Department of Physics and Astronomy, The University of Kansas, Lawrence, Kansas 66045, USA. E-mail: huizhao@ku.edu; Fax: +1 785 864 5262; Tel: +1 785 864 1938*

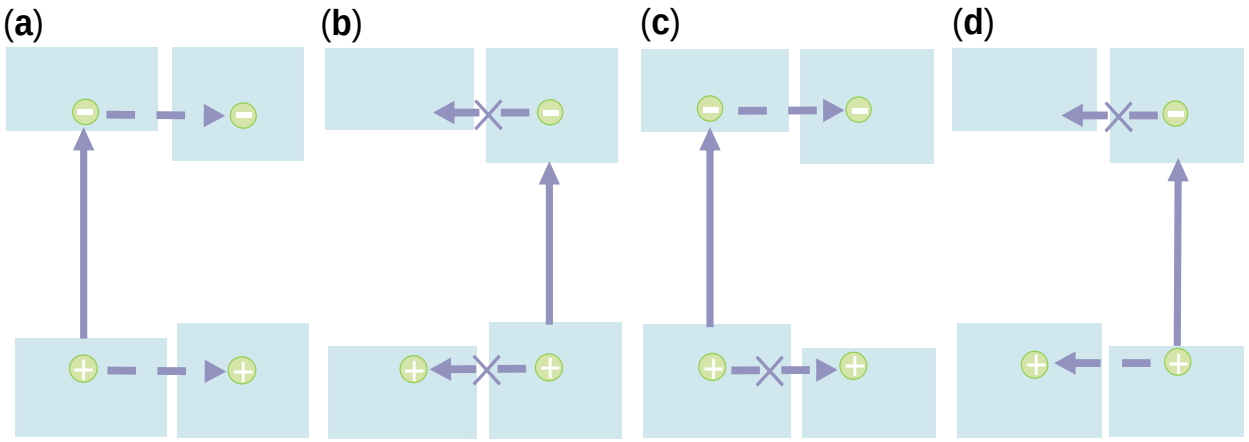

Fig. 1 Schematic of the band alignment between two semiconductors, showing type-I (a and b) and type-II (c and d) alignments.

have been identified, including MoS_2/ReS_2 [10], $WSe_2/MoTe_2$ [11], PbI2/WS_2 [12], and $WSe_2/PtSe_2$ [13]. Consequently, there is an urgent need to explore additional type-I vdW interfaces to broaden the applications of these materials. Discovery of new type-I interfaces will also facilitate the design and fabrication of multilayer heterostructures with intricate band alignment landscapes.

Here, we investigate the type-I interface formed between a newly discovered 2D semiconductor, $PdSe_2$, and monolayer WS_2, a well-known prototype in the field. $PdSe_2$ has garnered significant attention as an individual material due to its unique properties. Its orthorhombic structure exhibits a distinctive corrugated pentagonal configuration, with each layer composed of three atomic facets. The central Pd atom establishes covalent bonds with four Se atoms in the upper and lower sublayers [14,15], resulting in a rare folded pentagonal structure. This low-symmetry lattice arrangement imparts $PdSe_2$ with remarkable physical properties, making it highly sought after in various research domains [16]. One notable attribute of $PdSe_2$ is its high carrier mobility, enabling efficient charge transport and rendering it suitable for high-performance electronic devices [17]. Additionally, the bandgap of $PdSe_2$ can be finely tuned by adjusting its thickness, allowing for operation across a wide spectral range from deep ultraviolet to mid-infrared [18]. This tunability, coupled with its high carrier mobility, positions $PdSe_2$ as a promising candidate for thermoelectric materials in energy conversion and thermal management applications [16,19]. Furthermore, $PdSe_2$ displays magnetic transport properties, offering potential applications in magnetic and memory devices [20]. Beyond its physical characteristics, $PdSe_2$ exhibits excellent air stability [18], retaining its properties and structure under typical atmospheric conditions [14]. It also demonstrates high photoresponsivity, enabling rapid response to optical signals and making it well-suited for various optoelectronic applications. Moreover, its exceptional nonlinear optical responses and in-plane optical anisotropy make it a promising candidate for optical and photonic devices [21,22]. Consequently, air-stabilized $PdSe_2$ has found applications in electronic and photonic devices. Researchers have employed techniques such as mechanical stripping and chemical synthesis to utilize $PdSe_2$ in field-effect transistors [23], gas sensors [24], catalysts [25,26], energy storage and harvesting devices [27], photodetectors [22,28], photo-modulators [29,30], thermoelectric materials, and a wide array of other electronic and photonic devices [31–33].

Previously, attempted have been made to combined 2D $PdSe_2$ with other vdW materials to form heterostructures, such as $MoSe_2$ [34], WS_2 [35], InSe [36], MoS_2 [37], and $MoTe_2$ [38]. Although there have been reports that both $PdSe_2$ and PtS_2 can form Type I heterostructures with WS_2 crystals [35,39]. However, the discussion surrounding the underlying physical mechanisms governing the electronic properties of these heterostructures remains limited. Notably, the interlayer charge transfer process plays a pivotal role in realizing the exceptional electronic and optical properties of vdWHs. By manipulating interlayer charge transfer, it becomes possible to modify the electronic properties, light absorption characteristics, and surface active sites of $PdSe_2$-based heterostructures. Such control directly impacts the performance of various devices. For instance, it influences the sensitivity and efficiency of photodetectors and optical modulators [21], the reactivity and selectivity of catalysts [40], as well as the energy conversion and storage capabilities of batteries and supercapacitors [41]. Moreover, the precise control and modulation of electrons across distinct layers open up exciting possibilities for the design of innovative nanoelectronic devices, including transistors, logic gates, and quantum bits [33]. Despite the importance of this issue for many application, the interlayer charge transfer between $PdSe_2$ and other 2D materials has been rarely studied so far.

In this study, the interlayer electron and hole transfer between a trilayer $PdSe_2$ and a monolayer WS_2 was experimentally investigated. The characterization of the $WS_2/PdSe_2$ heterostructure was performed using photoluminescence (PL) spectroscopy. The results revealed a significant quenching of approximately 98% in the A-exciton emission intensity of WS_2 within the heterostructure. This reduction in emission intensity suggests the occurrence of interlayer excitation transfer from WS_2 to $PdSe_2$. Transient absorption measurements showed that both interlayer electron and hole transfers occur within the heterostructure on a picosecond timescale. When exciting the $PdSe_2$ layer, it was observed that electrons and holes do not transfer to WS_2 but instead remain within the $PdSe_2$ layer. These experimental results establish a

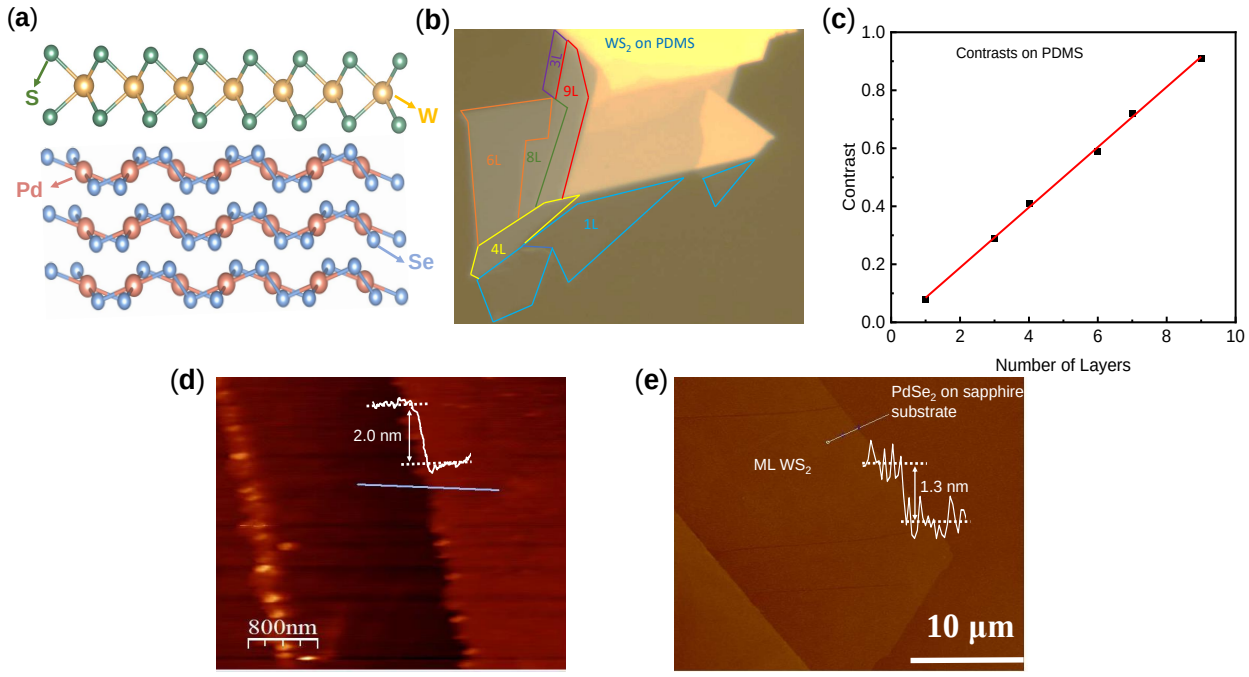

Fig. 2 Characterization of $WS_2/PdSe_2$ heterostructure. (a) Schematics of a $WS_2/PdSe_2$ heterostructure formed by vertically stacking together monolayers of WS_2 (top) and trilayer $PdSe_2$ (bottom). (b) Optical microscope image of WS_2 flakes on a PDMS substrate. Regions with different contrasts are assigned to different numbers of layers. (c) Green-channel contrast of the regions labeled in (b) as a function of the assigned layer number. The red line is a linear fit. (d) Atomic force microscope image of the $PdSe_2$ sample. (e) Atomic force microscope image of the fabricated $WS_2/PdSe_2$ heterostructure sample. The overall increase of background height with position, which is due to instrumentation calibration issue, has been removed to show the height of the sample.

type-I band alignment in the $WS_2/PdSe_2$ heterostructure.

2 Results and Discussion

2.1 Preparation and characterization of $WS_2/PdSe_2$ heterostructure

Figure 2a illustrates the schematic representation of the monolayer WS_2/trilayer $PdSe_2$ heterostructure. We employed a dry transfer technique to stack a monolayer WS_2 flake onto a trilayer $PdSe_2$ film. The monolayer WS_2 flakes were obtained through mechanical exfoliation, wherein large WS_2 crystals (acquired from 2D Semiconductors) were pressed onto a transparent polydimethylsiloxane (PDMS) substrate using a tape and then swiftly peeled off. To identify the monolayer flakes based on their optical contrast, we examined the flakes on the PDMS substrate under an optical microscope. It has been well established that for a thin film on a thick and transparent substrate, its contrast is proportional to its thickness [42].Figure 2b shows an optical microscope image of some WS_2 flakes on a PDMS substrate, which shows regions with different contrasts. For each region, we calculate its contrast, which is defined as the difference in the green-channel counts between the flake and bare PDMS substrate, divided by the latter. Figure 2c shows the calculated contrast as a function of the assigned layer numbers. A clear steplike feature of the contrast is observed. Therefore, we can safely use the step (0.1) as the monolayer contrast and unambiguously identify monolayer WS_2 regions.

The trilayer $PdSe_2$ film used in this study was synthesized on a c-cut sapphire substrate using chemical vapor deposition method (acquired from 6 Carbon Technology Corp.). To confirm its thickness, atomic force microscopy (AFM) is performed, as shown in Figure 2d. A line-cut shows the step of 2.0 nm from the sapphire substrate to $PdSe_2$, which agrees with previously reported monolayer $PdSe_2$ thickness of 0.6 nm [23].

To obtained the heterostructure sample, a selected WS_2 monolayer flake is transferred onto the trilayer $PdSe_2$ film. To improve the interface quality, the samples were thermally annealled at 150 °C for 2 hours in an Ar/H_2 (100 sccm/5 sccm) environment at a base pressure of approximately 2 Torr. The hot annealing process is crucial for obtaining a good interface through a self-cleaning mechanism, in which van der Waals forces induce the aggregation of interface pollutants into bubble-like structures. At high temperatures, impurities such as bubbles will undergo physical movement and tend to aggregate into larger bubbles at larger intervals, pushing them (as well as pollutants captured internally) to the edge of the sample and eliminating them [43–45]. This helps to obtain a sufficiently large, clean, and atomically flat area for experimental purposes without the need for external chemical treatment or cleaning. Figure 2e shows the heterostructure sample obtained by transferring the identified monolayer WS_2 wafer onto a double-sided polished sapphire substrate completely covered with $PdSe_2$. As $PdSe_2$ is completely covered on a double-sided polished sapphire substrate, the AFM image shows clear monolayer WS_2 profile. A line-cut shows the step of 1.3 nm from the WS_2 to

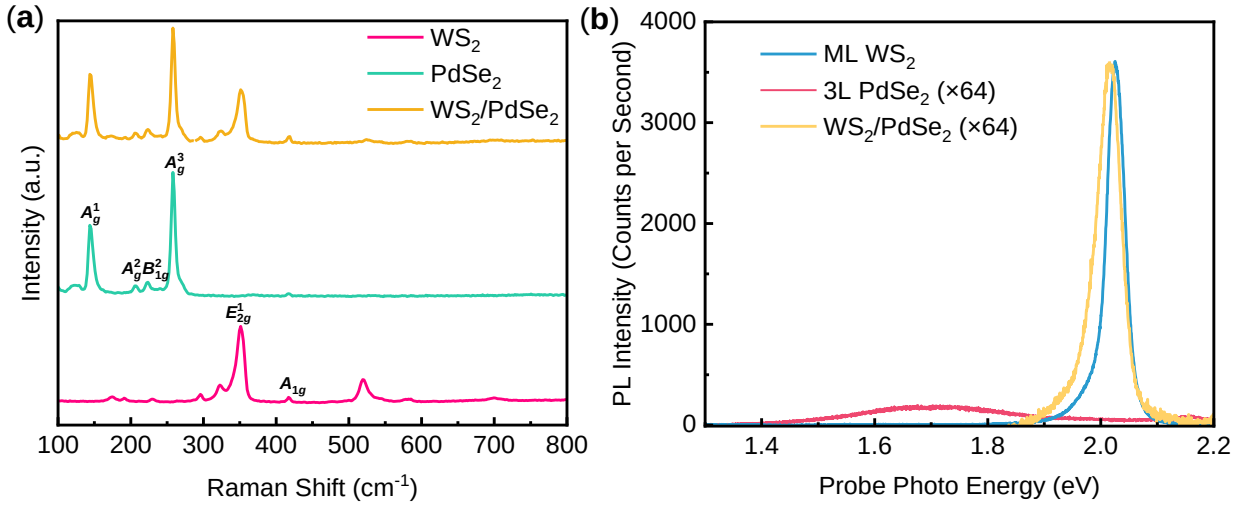

Fig. 3 (a) Raman spectra of monolayer WS_2, trilayer $PdSe_2$ and the $WS_2/PdSe_2$ heterostructure. (b) Photoluminescence spectra of the heterostructure sample, trilayer $PdSe_2$ and of the monolayer WS_2 flake before its transfer to $PdSe_2$.

$PdSe_2$, the thickness from line cut is more than WS_2 monolayer (0.7 nm)but less than bilayer[46], so it must be a monolayer.

The sample was characterized by Raman spectroscopy. Figure 3a displays the Raman spectra measured from three distinct regions. The spectrum of the monolayer WS_2 region clearly exhibits two characteristic peaks corresponding to the in-plane (E^1_{2g}, 352 cm^{-1}) and out-of-plane (A_1g, 419 cm^{-1}) vibration modes[47], confirming the WS_2 crystal structure. Notably, the characteristic WS_2 peaks in the heterostructure region align with those of the monolayer WS_2, suggesting that the dry transfer and thermal annealing processes have minimal impact on the lattice properties of WS_2. The Raman spectrum of the $PdSe_2$ region reveals four peaks associated with the vibrational modes A^1_g, A^2_g, B^2_{1g} and A^3_g, with frequencies at 144, 206, 222, and 257 cm^{-1}, respectively. These characteristic peaks align with the spectroscopic results reported in the literature for $PdSe_2$[14]. In the heterostructure region, all these characteristic peaks are clearly observed, further confirming the high quality of the heterostructure samples.

PL spectroscopic measurements were conducted to investigate the interfacial quality of the heterostructure sample and potential charge transfer processes. For comparison, an individual monolayer WS_2 sample was first studied, using a continuous-wave 2.33-eV laser beam with a power of 2.6 μW. As shown in Figure 3b, a prominent peak at 2.01 eV (615 nm) was observed, which is consistent with previous results on monolayer WS_2[48]. The trilayer $PdSe_2$ has a relatively low PL intensity[49], as shown by the red line in Figure 3b. In the $WS_2/PdSe_2$ heterostructure, this peak is quenched by 64 times, as depicted as the yellow curve. Such a significant quenching shows that the photocarriers excited in the WS_2 layer of the heterostructure samples experience a much more efficient decay channel compared to those in individual WS_2 layer. This phenomenon can be attributed to transfer of electrons or holes or transfer of both electrons and holes, or excitons, from WS_2 to $PdSe_2$. Additionally, we observe a significant red shift of about 9 meV of the PL peak in the heterostructure compared to the individual WS_2 monolayer. Previously, this redshift has been attributed to the dielectric screening effect of the adjacent layer, which alters both the bandgap and the exciton binding energy of WS_2[50,51]. These PL results indicate the presence of a high-quality interface between the WS_2 and $PdSe_2$ layers in the heterostructure samples and show that at least one type of the photoexcited carriers can efficiently transfer to the trilayer $PdSe_2$ on a time scale that is much shorter than the recombination lifetime of excitons in WS_2.

2.2 Ultrafast electron and hole transfer from WS_2 to $PdSe_2$

The efficient excitation transfer from WS_2 to $PdSe_2$ established by PL spectroscopy can be achieved by different physical mechanisms, depending on the band alignment of this heterostructure. With a type-I band alignment, both electrons and holes are expected to transfer from WS_2 (the wide-gap material) to $PdSe_2$ (the narrow-gap material). This can be achieved by sequential transfer of electrons and holes, or excitonic transfer. On the other hand, if the band alignment is type-II, only one type of the carriers (electrons or holes) could transfer from WS_2 to $PdSe_2$, resulting in layer-separate electron and hole populations.

To study the mechanisms of the observed transfer process and the nature of the band alignment, we performed time-resolved transient absorption spectroscopy. In our homemade setup, a 3.02-eV (410 nm) pump pulse is focused onto the heterostructure region of the sample with a spot size of 1.8 μm. To probe the carrier dynamics, we used a probe pulse that is tuned to near the A-exciton resonance of WS_2. Since the pump photon energy exceeds the bandgaps of both layers, the pump excites electrons and holes on both sides of the interface. If the band alignment is type-I, we expect that the photoexcited electrons and holes will transfer from the WS_2 layer to the $PdSe_2$ layer.

We first measured the dependence of the peak differential reflectance (obtained when the probe pulse slightly delays the pump pulse) on the probe photon energy, as shown in Figure 4a. Here, the differential reflectance is defined as $\Delta R/R_0 = (R - R_0)/R_0$, where R and R_0 are the sample reflectance with and

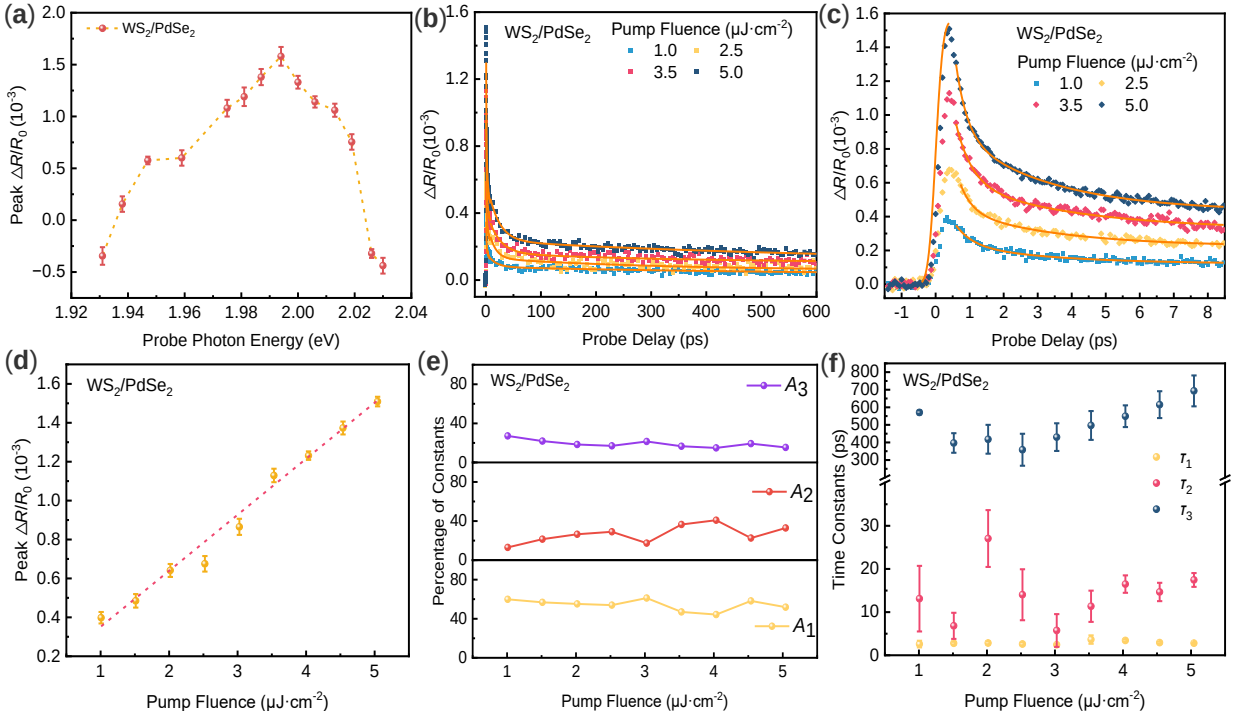

Fig. 4 (a) Peak differential reflectance as a function of the probe wavelength. (b) and (c) Differential reflectance of the $WS_2/PdSe_2$ heterostructure measured with 3.02 eV pump and 1.99 eV probe under various pump fluences as labeled. The orange curves are three-exponential fits. (d) Peak differential reflectance as a function of the pump fluence. The red line is a linear fit. (e) The weight of the decay component. (f) Decay time constants deduced from the three-exponential fits to the data.

without the pump presence, respectively. The pump fluence used in this measurement is 3.5 $\mu J\ cm^{-2}$. We observed a strong resonance characteristic near 2.0 eV, the A-exciton resonance of WS_2. The peak occurs at 1.99 eV (622 nm), which aligns well with the PL peak of the heterostructure.

We next performed time-resolved measurements with a 1.99-eV probe, which corresponds to the peak signal shown in Figure 4a, with various 3.02-eV pump fluences. The measured differential reflectance in long and short time ranges are shown in Figure 4b and 4c, respectively. The peak signal is proportional to the pump fluence, as confirmed by the linear fit shown in Figure 4d. The absorbance of monolayer WS_2 and trilayer $PdSe_2$ at the pump photon energy of 3.02 eV is 0.07[52] and 0.26[37], respectively. Based on these values, we estimate that the carrier densities injected in the WS_2 and $PdSe_2$ layers by a 1 $\mu J\ cm^{-2}$ pump pulse is approximately 1.4 and 4.6 $\times 10^{11}\ cm^{-2}$, respectively. The linear relation between the peak signal and the pump fluence (which is proportional to the injected carrier density) ensures that the evolution of the signal reflects the carrier dynamics.

As shown in Figure 4b and 4c, at each pump fluence, the signal raise to a peak on a timescale of approximately 0.39 ps, which is limited by the instrument response time. This shows that the carriers injected in the sample produces a peak differential reflectance signal instantaneously. The decay of the singal is fit by a tri-exponential function, $\Delta R/R_0 = A_1\exp(-t/\tau_1) + A_2\exp(-t/\tau_2) + A_3\exp(-t/\tau_3) + B$. Here, τ_1, τ_2 and τ_3 represent the decay time constants associated with different decay processes. A_1, A_2 and A_3 denote the weights of these processes, while B represents the weight of a time-independent background component. We plotted the weights of the different decay processes and the time constants against the pump fluence in Figures 4e and 4f. We observed a τ_1 process of approximately 1 ps, a τ_2 process of approximately 15 ps, and a very slow τ_3 process of several hundred ps.

To understand the origin of these processes, we repeated the measurement on the individual monolayer WS_2 sample with the same experimental condition and procedures. The results are plotted in Figure 5. Similar to the heterostructure sample, the peak differential reflectance signal show a strong resonant feature near the A-exciton line of WS_2 (Figure 5a). The time-resolved signal is plotted in Figure 5b and 5c, with a probe of 2.01 eV. The peak signal is also proportional to the pump fluence, as shown in Figure 5d. The decay of the signal is bi-exponential, with a short time constant of about 0.4 ps (Figure 5f), accounting for about 80% of the signal (Figure 5e), and a long time constant of about 15 ps. Previous studies have well established that under these conditions, the 0.4-ps process is due to the exciton formation from the injected free electron-hole pairs, while the 15-ps process is from the exciton recombination[53]. Hence, we can assign the τ_1 and τ_2 processes observed in the heterostructure sample to these carrier dynamics in its WS_2 layer.

The major difference observed between the heterostructure and the WS_2 monolayer samples is the presence of a slow process with a timescale of 400 ps in the heterostructure. This slow component could have two possible origins. If the band alignment of the heterostructure is type-II, one type of carriers (either electrons or holes) would predominantly reside in the WS_2 layer,

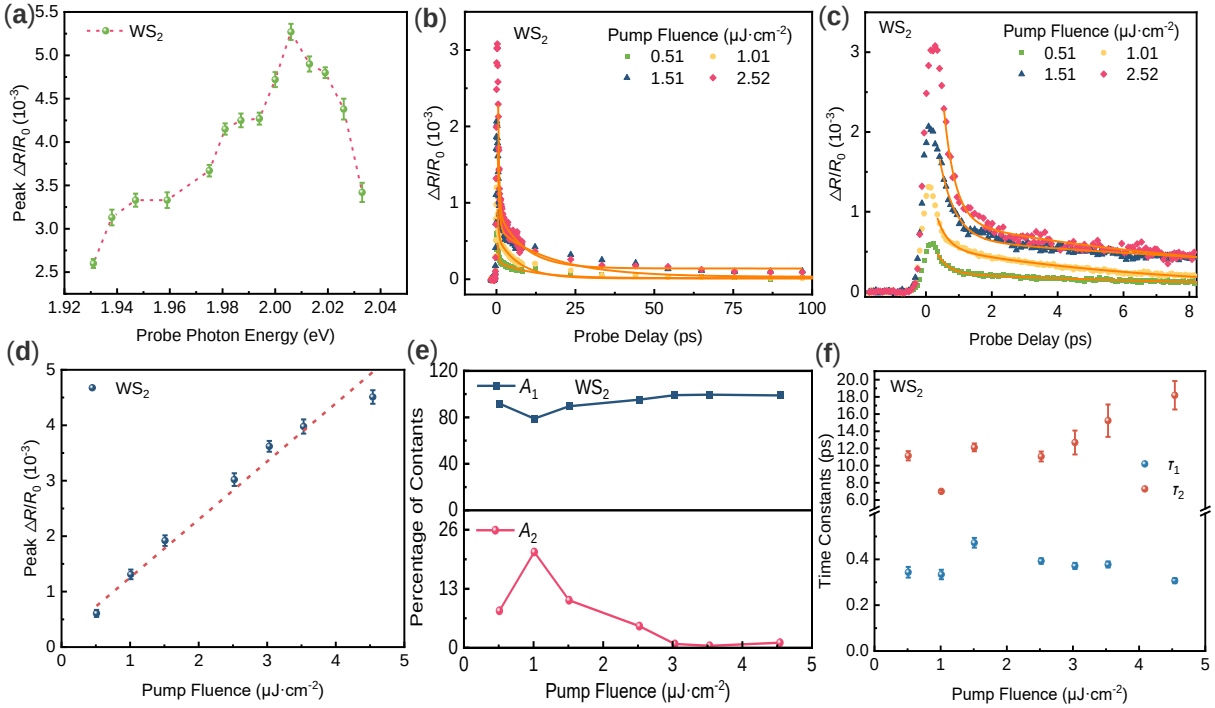

Fig. 5 (a) Peak differential reflectance as a function of the probe wavelength. (b) and (c) Differential reflectance of the monolayer WS_2 measured with a 3.02 eV pump and 2.01 eV probe under various pump fluences as labeled. The orange curves are bi-exponential fits. (d) Peak differential reflectance as a function of the pump fluence. The red line is a linear fit. (e) The weight of the decay component. (f) Decay time constants deduced from the bi-exponential fits to the data.

while the other type would be localized in the $PdSe_2$ layer. Due to the spatial separation of these carriers, their recombination lifetime would be relatively long. Alternatively, if the band alignment within the heterostructure is type-I, both types of carriers would efficiently transfer to the $PdSe_2$ layer. In this case, the carriers in the $PdSe_2$ layer could produce a long-lived signal if they have a prolonged lifetime due to the indirect bandgap of $PdSe_2$.

To distinguish these two possible origins, we next performed a comparison study of monolayer WS_2, trilayer $PdSe_2$, and the heterostructure. Figure 6a, 6b, and 6c shows the time-resolved differential reflectance signal obtained with the sample 3.02-eV pump of 3.1 $\mu J\ cm^2$, and with various probe wavelengths, as labeled. Interestingly, the long-lived component of the signal exists in both the heterostructure and the $PdSe_2$ samples. To better analyze the effect of the probe photon energy, we plot the signal as a function of the probe photon energy at 3 probe delays for each sample in Figure 6d, 6e, and 6f. The signal from $PdSe_2$ show a peak in the range of 1.95-1.98 eV (Figure 6e). The origin of this feature is unclear; however, at late probe delays (500 ps), the signal shows no dependence on the probe photon energy in this range. This is reasonable since the probe photon energy is much larger than the bandgap of trilayer $PdSe_2$. The peak signal and that at 2 ps from the heterostructure show a peak corresponding to monolayer WS_2 and a secondary peak that resembles the $PdSe_2$ peak.

The comparison measurement is establishes that the long-lived signal observed in the heterostructure sample does not exhibit any dependence on the probe photon energy. This observation is crucial because if the band alignment were type-II and the signal component originated from one type of carriers in WS_2, it would be expected to show a resonant feature near the A-exciton line of WS_2 (as shown in Figure 6f). However, the absence of this resonant feature, coupled with the similarity of the signal to that from the $PdSe_2$ sample, provides strong evidence that the long-lived signal in the heterostructure originates from carriers in the $PdSe_2$ layer. This finding supports the hypothesis that the heterostructure has a type-I band alignment, where the photoexcited electrons and holes both transfer to the $PdSe_2$ layer, resulting in a prolonged recombination lifetime. Furthermore, the two short decay time constants of the heterostructure are similar to those in monolayer WS_2, which correspond to exciton formation and recombination processes, respectively. This shows that the electron and hole transfer process from WS_2 to $PdSe_2$ occurs on an ultrafast time scale that convolutes with the exciton formation process. Otherwise, an additional decay process would have been observed in the heterostructure.

2.3 Lack of carrier transfer from $PdSe_2$ to WS_2

To further confirm the type-I band alignment in the $WS_2/PdSe_2$ heterostructure and validate the absence of charge transfer from WS_2 to $PdSe_2$, an alternate pump and probe configuration was employed. This configuration utilized a pump photon energy of 1.52 eV (equivalent to 820 nm), which was not sufficient to excite the WS_2 layer. Therefore, the photoexcited carriers were only injected into the $PdSe_2$ layer. Subsequently, a probe photon with an energy of 2.01 eV (corresponding to 620 nm) was utilized to

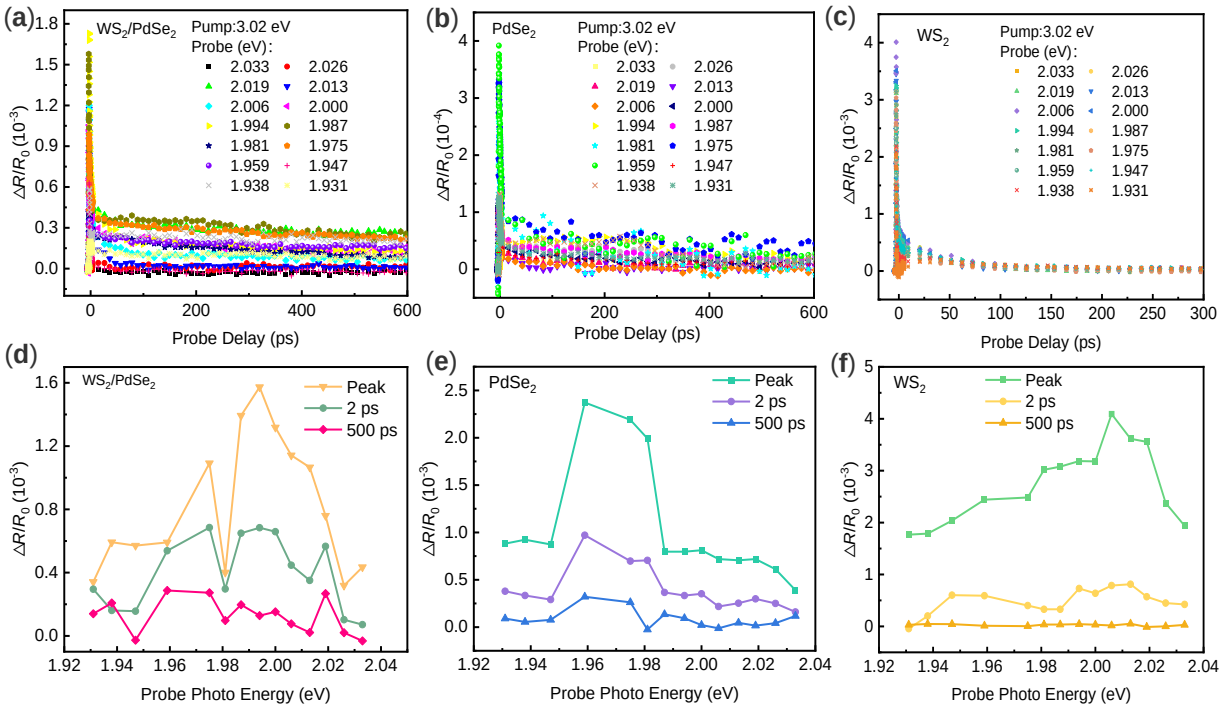

Fig. 6 (a),(b) and (c) are the $WS_2/PdSe_2$ heterostructure, trilayer $PdSe_2$ and monolayer WS_2 measured with a 3.02 eV pump and probe pulses wavelength dependence. (d),(e)and (f) Peak values of the $WS_2/PdSe_2$ heterostructure, trilayer $PdSe_2$ and monolayer WS_2 at different wavelengths, as well as the values of the differential reflection signals at 2 ps and 500 ps.

resonantly match the A-exciton in the monolayer WS_2, primarily detecting carriers in the WS_2 layer. The resulting differential reflectance signals are presented in Figure 7a (long range) and 7b (short range). These figures clearly demonstrate that the signal from the heterostructure closely resembles that of the trilayer $PdSe_2$. Importantly, no signal is detected from the monolayer WS_2 sample (indicated by the orange symbols in Figure 7b), confirming that it remains unexcited under this pump and probe configuration. If the energy band alignment were type II, electrons or holes would transfer from $PdSe_2$ to WS_2, resulting in a significantly different signal compared to that of the trilayer $PdSe_2$. However, the similarity between the heterostructure and the trilayer $PdSe_2$ signals confirms the absence of charge transfer from WS_2 to $PdSe_2$ in the heterostructure. This experimental result provides further evidence supporting the type-I band alignment of the $WS_2/PdSe_2$ heterostructure, where carriers are predominantly confined within the $PdSe_2$ layer and do not transfer to the WS_2 layer.

Finally, the measurements were repeated on the heterostructure sample using various probe photon energies. The results, depicted in Figure 7c, 7d, and 7e, showed that the differential reflectance signal remained constant regardless of the probe photon energy. This observation provides further confirmation of the absence of carrier population in WS_2. If there were carriers present in WS_2, the differential reflectance induced by these carriers would exhibit pronounced resonant features within the range of photon energies used in the measurement.

3 Conclusion

In this study, a comprehensive investigation was conducted to analyze the energy band arrangement and photocarrier dynamics in a vdWs heterostructure consisting of a monolayer WS_2 and a trilayer $PdSe_2$. The analysis involved the use of PL and transient absorption spectroscopy techniques. Notably, in the heterostructure samples, a significant quenching effect was observed in the PL of WS_2, indicating efficient excitation transfer from WS_2 to $PdSe_2$. Transient absorption measurements with reflective geometry provided strong evidence of the type-I band alignment in this heterostructure. Through selective excitation and probing of photocarriers in different layers of the heterostructures and comparing them with individual WS_2 and $PdSe_2$ samples, it was found that both electrons and holes excited in WS_2 transfer to $PdSe_2$ and eventually recombine within $PdSe_2$. However, neither electrons nor holes excited in $PdSe_2$ were observed to transfer to WS_2. These insights into the charge transfer properties of the heterostructure are crucial for the design and fabrication of 2D heterostructures with unique properties and for optimizing the performance of $PdSe_2$-based heterostructures in optoelectronic devices.

4 Experimental

Raman and PL spectroscopy: Raman and PL spectroscopy measurements were conducted using a LabRAM HR Evolution Raman spectrometer (Horiba Jobin Yvon, Japan) equipped with a 532 nm continuous wave excitation source. The excitation light was focused onto the samples using a 50x objective lens, resulting in a spot size of approximately 1.8 μm. To ensure consistency, all

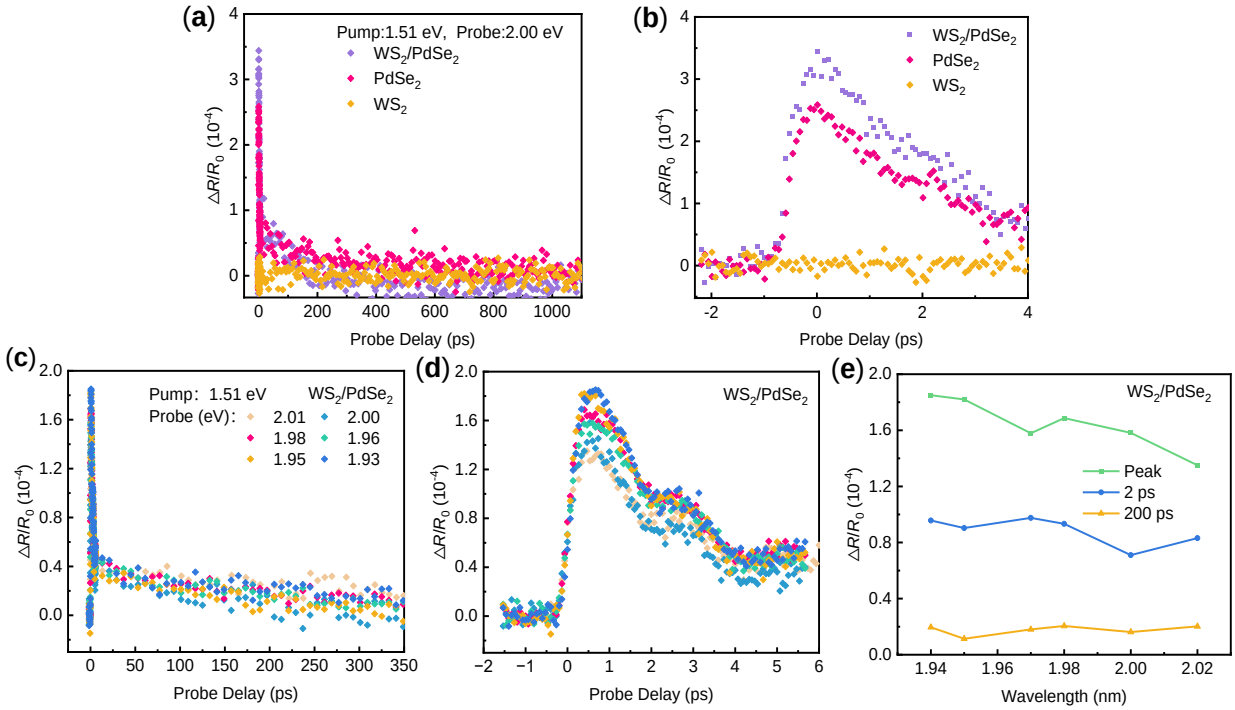

Fig. 7 (a) and (b) Differential reflectance of the $WS_2/PdSe_2$ heterostructure, trilayer $PdSe_2$ and monolayer WS_2 measured with 1.51 eV pump and 2.00 eV probe. (c) and (d) are the $WS_2/PdSe_2$ heterostructure measured with 1.51 eV pump and probe pulses wavelength dependence. (e) Peak values of the $WS_2/PdSe_2$ heterostructure at different wavelengths, as well as the values of the differential reflection signals at 2 ps and 200 ps.

spectra were acquired under identical experimental conditions.

Transient Absorption Measurements: In transient absorption measurements using reflective geometry, the probe beam is aligned with the pump beam to interrogate the sample's surface. A Newport Ti: Sapphire laser is employed, generating a 100 fs femtosecond laser pulse with a repetition frequency of 80 MHz and a wavelength of 820 nm. The laser pulse is divided into two parts: one part pumps an OPO (optical parametric oscillator) to produce pulses within the 490-750 nm range, while the other part is focused into a barium borate (BBO) crystal to generate the second harmonic, a 410 nm pump laser pulse used for sample excitation. Alternatively, this part of the 820 beam can be directly used in the experiment as a pump pulse. The pump and probe light pulses are sent into the same optical path through a beam splitter. The two beams are focused onto the sample surface using a microscope objective with a numerical aperture of 0.4. The reflected pump beam from the sample is obstructed by a set of color filters, while the reflected probe beam retraces its path, passing through the microscope objective again before being detected by a silicon photodiode connected to a lock-in amplifier. The voltage of the detector is measured and presented using a lock-in amplifier, which operates in synchronization with a light chopper positioned along the path. This light chopper modulates the intensity of the pump light directed towards the sample at a frequency of approximately 2 kHz. To manipulate the relative positions of the pump and the probe as they reach the sample, a motorized translational stage with a retroreflector is employed in the experimental setup. This arrangement allows for adjustments in the delay of the probe pulse relative to the pump pulse. The change in normalized probe reflectivity, expressed as the differential reflectivity $\Delta R/R_0 = (R - R_0)/R_0$ is measured. Here, R and R_0 represent the probe reflectivity in the presence and absence of the pump light, respectively. All measurements are conducted at room temperature with the sample exposed to air, and no degradation of the sample is observed throughout the study.

Conflicts of interest

The authors declare no conflict of interest.

Data availability

All relevant data are within the paper.

Acknowledgements

The authors thanks the financial support of the National Key R&D Program of China (Grant Nos.2023YFA1407200 and 2023YFA1407201), National Natural Science Foundation of China (Grant Nos.11974088 and 61975007), the Beijing Natural Science Foundation (Grant No. 4222073). H.Z. acknowledges support by the U.S. Department of Energy (DE-SC0020995).

Notes and references

1 S. Zhang, J. Liu, M. M. Kirchner, H. Wang, Y. Ren and W. Lei, *Journal of Physics D: Applied Physics*, 2021, **54**, 433001.
2 X. Zhou and G. Yu, *ACS nano*, 2021, **15**, 11040–11065.
3 H.-S. Ra, S.-H. Lee, S.-J. Jeong, S. Cho and J.-S. Lee, *Small Methods*, 2024, **8**, 2300245.
4 S. Joseph, J. Mohan, S. Lakshmy, S. Thomas, B. Chakraborty,

S. Thomas and N. Kalarikkal, *Materials Chemistry and Physics*, 2023, **297**, 127332.
5 L.-X. Wang, C. G. Tang, Z.-S. Tan, H.-Y. Phua, J. Chen, W. Lei, R.-Q. Png, L.-L. Chua and P. K. Ho, *Materials Horizons*, 2022, **9**, 2147–2159.
6 S. Ahmad, K. Sohail, L. Chen, H. Xu, H. Din and Z. Zhou, *International Journal of Hydrogen Energy*, 2023, **48**, 25354–25365.
7 W. Ahmad, L. Pan, K. Khan, L. Jia, Q. Zhuang and Z. Wang, *Advanced Functional Materials*, 2023, **33**, 2300686.
8 H. Gao, C. Du, J. Sun, J. Zhang, J. Leng, J. Li, W. Wang and K. Li, *Materials Today Communications*, 2023, **35**, 105959.
9 R. Sakthivel, M. Keerthi, R.-J. Chung and J.-H. He, *Progress in Materials Science*, 2023, **132**, 101024.
10 M. Z. Bellus, M. Li, S. D. Lane, F. Ceballos, Q. Cui, X. C. Zeng and H. Zhao, *Nanoscale Horizons*, 2017, **2**, 31–36.
11 L. Ming, B. Matthew, D. Jun, M. Liang, L. Xiuling, Z. Hui and Z. X. Cheng, *Nanotechnology*, 2018, **29**, year.
12 W. Zheng, B. Zheng, Y. Jiang, C. Yan, S. Chen, Y. Liu, X. Sun, C. Zhu, Z. Qi, T. Yang *et al.*, *Nano letters*, 2019, **19**, 7217–7225.
13 P. Wang, Y. Wang, A. Bian, S. Hao, Q. Miao, X. Zhang, J. He, D. He and H. Zhao, *2D Materials*, 2022, **9**, 035019.
14 A. D. Oyedele, S. Yang, L. Liang, A. A. Puretzky, K. Wang, J. Zhang, P. Yu, P. R. Pudasaini, A. W. Ghosh, Z. Liu *et al.*, *Journal of the American Chemical Society*, 2017, **139**, 14090–14097.
15 L.-H. Zeng, D. Wu, S.-H. Lin, C. Xie, H.-Y. Yuan, W. Lu, S. P. Lau, Y. Chai, L.-B. Luo, Z.-J. Li *et al.*, *Advanced Functional Materials*, 2019, **29**, 1970005.
16 A. A. Puretzky, A. D. Oyedele, K. Xiao, A. V. Haglund, B. G. Sumpter, D. Mandrus, D. B. Geohegan and L. Liang, *2D Materials*, 2018, **5**, 035016 (12pp).
17 Y. Wang, Y. Li and Z. Chen, *Journal of Materials Chemistry C*, 2015, **3**, 9603–9608.
18 Q. Liang, Q. Wang, Q. Zhang, J. Wei, S. X. Lim, R. Zhu, J. Hu, W. Wei, C. Lee, C. Sow *et al.*, *Advanced Materials*, 2019, **31**, 1807609.
19 S. Deng, L. Li and Y. Zhang, *Acs Applied Nano Materials*, 2018, **1**, 1932–1939.
20 R. Zhu, Z. Gao, Q. Liang, J. Hu, J.-S. Wang, C.-W. Qiu and A. T. S. Wee, *ACS Applied Materials & Interfaces*, 2021, **13**, 37527–37534.
21 G. Li, S. Yin, C. Tan, L. Chen, M. Yu, L. Li and F. Yan, *Advanced Functional Materials*, 2021, **31**, 2104787.
22 M. Long, Y. Wang, P. Wang, X. Zhou, H. Xia, C. Luo, S. Huang, G. Zhang, H. Yan, Z. Fan *et al.*, *Acs Nano*, 2019, **13**, 2511–2519.
23 Wai, Leong, Chow, Peng, Yu, Fucai, Liu, Jinhua, Hong and Xingli, *Advanced Materials*, 2017.
24 X. J. Min, J. W. Zhao, W. W. Qin, L. B. Luo, W. Zhang, J. L. Fan, X. F. Hu and C. Fu, *ACS Applied Nano Materials*, 2021, **4**, 7358–7370.
25 J. Li, D. Liang, G. Liu, B. Jia, J. Cao, J. Hao and P. Lu, *RSC advances*, 2021, **11**, 38478–38485.
26 R. Song, L. Wang and Y. Li, *Applied Surface Science*, 2022, **597**, 153626.
27 Y. Li, S. Chen, Z. Yu, S. Li, Y. Xiong, M.-E. Pam, Y.-W. Zhang and K.-W. Ang, *Advanced Materials*, 2022, **34**, 2201488.
28 Q. Liang, Q. Wang, Q. Zhang, J. Wei, S. X. Lim, R. Zhu, J. Hu, W. Wei, C. Lee and C. H. Sow, *Advanced Materials*, 2019, **31**, year.
29 V. K. Gudelli and G. Y. Guo, *New Journal of Physics*, 2021, **23**, 093028 (15pp).
30 N. Xu, X. Shang, F. Yang, Z. Sui, H. Zhang and D. Li, *Infrared Physics & Technology*, 2023, **131**, 104626.
31 L.-S. Lu, G.-H. Chen, H.-Y. Cheng, C.-P. Chuu, K.-C. Lu, C.-H. Chen, M.-Y. Lu, T.-H. Chuang, D.-H. Wei, W.-C. Chueh *et al.*, *ACS nano*, 2020, **14**, 4963–4972.
32 M. Sun, J. P. Chou, L. Shi, J. Gao and G. Zhang, *ACS Omega*, 2018, **3**, 5971–5979.
33 Y. Zhao, P. Yu, G. Zhang, M. Sun, D. Chi, K. Hippalgaonkar, J. T. Thong and J. Wu, *Advanced Functional Materials*, 2020, **30**, 2004896.
34 M. Jakhar, J. Singh, A. Kumar and K. Tankeshwar, *Nanotechnology*, 2019, **31**, year.
35 X. Kang, C. Lan, F. Li, W. Wang, S. Yip, Y. Meng, F. Wang, Z. Lai, C. Liu and J. C. Ho, *Advanced Optical Materials*, 2021, **9**, 2001991.
36 W. Ahmad, J. Liu, J. Jiang, Q. Hao, D. Wu, Y. Ke, H. Gan, V. Laxmi, Z. Ouyang, F. Ouyang *et al.*, *Advanced Functional Materials*, 2021, **31**, 2104143.
37 H. Gao, C. Du, L. Chen, W. Wang and K. Li, *Advanced Materials Interfaces*, 2022, **9**, 2102350.
38 A. M. Afzal, M. Z. Iqbal, G. Dastgeer, A. u. Ahmad and B. Park, *Advanced Science*, 2021, **8**, 2003713.
39 Z. Wang, H. Zhang, W. Wang, C. Tan, J. Chen, S. Yin, H. Zhang, A. Zhu, G. Li, Y. Du *et al.*, *ACS Applied Materials & Interfaces*, 2022, **14**, 37926–37936.
40 Z. Lin, B. Xiao, Z. Wang, W. Tao, S. Shen, L. Huang, J. Zhang, F. Meng, Q. Zhang, L. Gu *et al.*, *Advanced Functional Materials*, 2021, **31**, 2102321.
41 Y. Wang, J. Pang, Q. Cheng, L. Han, Y. Li, X. Meng, B. Ibarlucea, H. Zhao, F. Yang, H. Liu *et al.*, *Nano-Micro Letters*, 2021, **13**, 143.
42 B. Aslan, D. A. Chenet, A. M. Van Der Zande, J. C. Hone and T. F. Heinz, *Acs Photonics*, 2015, **3**, 96–101.
43 S. J. Haigh, A. Gholinia, R. Jalil, S. Romani, L. Britnell, D. C. Elias, K. S. Novoselov, L. A. Ponomarenko, A. K. Geim and R. Gorbachev, *Nature materials*, 2012, **11**, 764–767.
44 D. G. Purdie, N. Pugno, T. Taniguchi, K. Watanabe, A. Ferrari and A. Lombardo, *Nature communications*, 2018, **9**, 5387.
45 Y. Kim, P. Herlinger, T. Taniguchi, K. Watanabe and J. H. Smet, *ACS nano*, 2019, **13**, 14182–14190.
46 W. Zhao, Z. Ghorannevis, L. Chu, M. Toh, C. Kloc, P.-H. Tan and G. Eda, *ACS nano*, 2013, **7**, 791–797.
47 M. Virsek, A. Jesih, I. Milosevic, M. Damnjanovic and M. Remskar, *Surface Science*, 2007, **601**, 2868–2872.

48 W. Shi, M. L. Lin, Q. H. Tan, X. F. Qiao and P. H. Tan, *2D Materials*, 2016, **3**, 025016.

49 Z. Lei, X. Zhang, Y. Zhao, A. Wei, L. Tao, Y. Yang, Z. Zheng, L. Tao, P. Yu and J. Li, *Nanoscale*, 2022, **14**, 4181–4187.

50 K. Kośmider and J. Fernández-Rossier, *Physical Review B*, 2013, **87**, 075451.

51 H.-P. Komsa and A. V. Krasheninnikov, *Physical Review B*, 2013, **88**, 085318.

52 J. Schmeink, V. Musytschuk, E. Pollmann, S. Sleziona, A. Maas and M. Schleberger, *arXiv e-prints*, 2021.

53 J. He, D. He, Y. Wang, Q. Cui, F. Ceballos and H. Zhao, *Nanoscale*, 2015, **7**, 9526–9531.

Data availability statement

- All relevant data are within the manuscript and the data supporting this article have been included as part of the Supplementary Information.

.